Pancharatnam–Berry phase engineering from spin duality to spin selectivity for optical vortex generation

Siming Li(林思铭), Jing Wang(王静), Shiwei Tang(汤世伟)

Citation: Chin. Phys. B. 35, 104211 (2026). DOI: 10.1088/1674-1056/aeac04 | CSTR: 32038.14.CPB.aeac04
http://cpb.iphy.ac.cn; http://iopscience.iop.org/cpb

What follows is a list of articles you may be interested in

Generation of elliptical airy vortex beams based on all-dielectric metasurface

Xiao-Ju Xue(薛晓菊), Bi-Jun Xu(徐弼军), Bai-Rui Wu(吴白瑞), Xiao-Gang Wang(汪小刚), Xin-Ning Yu(俞昕宁), Lu Lin(林露), Hong-Qiang Li(李宏强)
Chin. Phys. B. 32, 024215 (2023). DOI: 10.1088/1674-1056/ac7cd0

Asymmetrical photonic spin Hall effect based on dielectric metasurfaces

Guangzhou Geng(耿广州), Ruhao Pan(潘如豪), Wei Zhu(朱维), Junjie Li(李俊杰)
Chin. Phys. B. 31, 124207 (2022). DOI: 10.1088/1674-1056/ac754b

An ultra-wideband 2-bit coding metasurface using Pancharatnam—Berry phase for radar cross-section reduction

Bao-Qin Lin(林宝勤), Wen-Zhun Huang(黄文准), Lin-Tao Lv(吕林涛), Jian-Xin Guo(郭建新), Yan-Wen Wang(王衍文), Hong-Jun Ye(叶红军)
Chin. Phys. B. 31, 034204 (2022). DOI: 10.1088/1674-1056/ac11ec

Efficient manipulation of terahertz waves by multi-bit coding metasurfaces and further applications of such metasurfaces

Yunping Qi(祁云平), Baohe Zhang(张宝和), Jinghui Ding(丁京徽), Ting Zhang(张婷), Xiangxian Wang(王向贤), Zao Yi(易早)
Chin. Phys. B. 30, 024211 (2021). DOI: 10.1088/1674-1056/abd6fc

Hyperbolic metamaterials for high-efficiency generation of circularly polarized Airy beams

Lin Chen(陈林), Huihui Li(李会会), Weiming Hao(郝玮鸣), Xiang Yin(殷祥), Jian Wang(王健)
Chin. Phys. B. 29, 084210 (2020). DOI: 10.1088/1674-1056/ab96a1

SPECIAL TOPIC — A 40th Anniversary Celebration: Physics Research and Innovation at Ningbo University

Pancharatnam–Berry phase engineering from spin duality to spin selectivity for optical vortex generation

Siming Li(林思铭), Jing Wang(王静), and Shiwei Tang(汤世伟)[†]

School of Physical Science and Technology, Ningbo University, Ningbo 315211, *China*

(Received 30 July 2026; revised manuscript received 10 September 2026; accepted manuscript online 24 September 2026)

Pancharatnam–Berry (PB) metasurfaces provide a compact platform for spin-dependent wavefront manipulation, yet conventional birefringent designs generally allow both incident spin states to access the geometric phase. Here, we establish a unified Jones-matrix framework for PB-phase generation in reflective half-wave-plate-like (HWP-like), quarter-wave-plate-like (QWP-like), and non-Hermitian chiral-exceptional-point (chiral-EP) metasurfaces. The analysis shows that the rotation-induced PB phase appears in the off-diagonal channels of the reflection matrix expressed in a fixed laboratory-frame circular basis, while the local scattering response determines the accessibility of these channels. The HWP-like metasurface generates conjugate vortices under opposite circularly polarized incidences. The QWP-like metasurface produces a PB-modulated vortex together with an orthogonally polarized background without rotation-induced PB phase. Near a chiral EP, one off-diagonal channel remains finite while the opposite conversion channel is strongly suppressed, enabling incident-spin-selective optical-vortex generation. These results provide a unified description of birefringent and non-Hermitian PB metasurfaces and introduce spin-channel selectivity as an additional degree of freedom for geometric-phase wavefront control.

Keywords: Pancharatnam–Berry phase, optical metasurfaces, exceptional points, optical vortices

PACS: 42.25.Ja, 42.79.–e, 78.67.Pt

DOI: 10.1088/1674-1056/aeac04 **CSTR:** 32038.14.CPB.aeac04

1. Introduction

Optical metasurfaces composed of subwavelength artificial structures provide a compact platform for manipulating the amplitude, phase, polarization, and orbital angular momentum of light.[1–6] By engineering the local optical response of meta-atoms, metasurfaces have enabled anomalous reflection and refraction, focusing, holography, beam splitting, and optical-vortex generation. Their ultrathin configuration and flexible design make them attractive for optical communication, information processing, imaging, and spin-controlled photonic devices.[7–12] Furthermore, recent advances have also demonstrated the highly efficient generation of complex vectorial beams via surface-wave-excited metasurfaces.[13–15]

Among the available phase-control mechanisms, the Pancharatnam–Berry (PB) phase[11] is particularly useful because it can be encoded solely through the in-plane orientation of a meta-atom.[16,17] Under circularly polarized incidence, the rotation of a meta-atom introduces a spin-dependent phase into the cross-polarized component, thereby enabling efficient spin-to-orbital angular-momentum conversion and optical-vortex generation.[18–21] In a reflective half-wave-plate-like (HWP-like) PB metasurface, the two fixed laboratory-frame circular basis states are converted into each other and acquire geometric phases with opposite signs. Because reflection reverses the propagation direction, this conversion preserves the propagation-referenced circular handedness under the convention adopted here.[12,16,17,22] The two incident spin states therefore generate a pair of conjugate wavefronts with opposite topological charges.

Conventional birefringent PB metasurfaces nevertheless provide limited freedom for selecting the incident spin that can access the geometric phase. In an HWP-like system, both incident spins generally undergo efficient but symmetric spin conversion, producing conjugate outputs.[23–25] In a quarter-wave-plate-like (QWP-like) system, both diagonal and off-diagonal reflection channels contribute in the fixed circular basis. The off-diagonal component carries the rotation-induced PB phase, whereas the diagonal component provides a background without this geometric-phase modulation. The two reflected components have opposite circular handedness.[26] The geometric phase can therefore be encoded, but the incident-spin access to that phase is not intrinsically one-sided. Recently, specific symmetry-breaking designs have been proposed to break this fundamental spin duality, enabling spin-asymmetric geometric-phase responses.[27]

Non-Hermitian photonics introduces additional control through loss, gain, and asymmetric modal coupling.[28,29] Of particular interest are exceptional points (EPs), at which both eigenvalues and eigenvectors coalesce.[30] Such degeneracies can give rise to chiral mode conversion, asymmetric scattering,

[†]Corresponding author. E-mail: tangshiwei@nbu.edu.cn

© 2026 Chinese Physical Society and IOP Publishing Ltd. All rights, including for text and data mining, AI training, and similar technologies, are reserved.

enhanced sensitivity, and unidirectional response. Combining non-Hermitian EP physics with PB phase control may therefore provide a route to spin-selective geometric-phase excitation. In such a system, the PB phase is not only determined by the in-plane rotation of the meta-atom but can also be selectively activated or suppressed by the chiral scattering response near an exceptional point.[31–34] Recent cutting-edge studies have further demonstrated that EPs can topologically reconstruct PB phases for chiral spin–orbit interaction steering,[35] and such non-Hermitian topological transitions can even be dynamically tuned using active metasurface platforms.[36]

In this work, we theoretically establish a unified Jones-matrix description of PB-phase generation in reflective HWP-like, QWP-like, and chiral-exceptional-point (chiral-EP) metasurfaces, and numerically demonstrate their distinct optical-vortex responses at 600 nm. The HWP-like metasurface generates conjugate vortices under opposite circularly polarized incidences, whereas the QWP-like metasurface produces a PB-modulated vortex together with a diagonal channel background. The non-Hermitian design operates in the chiral-EP regime in which one off-diagonal channel is retained and the reverse channel is suppressed, thereby enabling spin-selective access to the PB phase. The comparison clarifies the common mathematical origin and different physical consequences of the three mechanisms.

2. Unified Jones-matrix framework

We first consider an unrotated anisotropic reflective meta-atom. In its local linear-polarization basis $\{\hat{u},\hat{v}\}$, the reflection Jones matrix is

$$R(0)=\begin{pmatrix} r_{uu} & r_{uv} \\ r_{vu} & r_{vv} \end{pmatrix}. \tag{1}$$

Here, u and v denote two orthogonal local in-plane coordinate axes. The coefficients r_{uu} and r_{vv} describe reflection into the same linear polarization, whereas r_{uv} and r_{vu} describe coupling between the two linear polarizations.

We adopt the time dependence $\exp(-\mathrm{i}\omega t)$ and a right-handed laboratory coordinate system (x,y,z). The states $|+\rangle = (1,\mathrm{i})^{\mathrm{T}}/\sqrt{2}$ and $|-\rangle = (1,-\mathrm{i})^{\mathrm{T}}/\sqrt{2}$ are defined using the same transverse laboratory axes for both incident and reflected fields. LCP and RCP denote counterclockwise and clockwise temporal rotation of the electric field, respectively, when viewed toward the source, opposite to the propagation direction. For incidence along $+z$, $|+\rangle$ and $|-\rangle$ correspond to LCP and RCP, respectively. For reflection along $-z$, these assignments are reversed. Thus, the $\pm$ labels denote fixed laboratory-frame circular basis states rather than propagation-referenced handedness.

The transformation to the fixed circular basis is given by $\tilde{R}(0)=UR(0)U^{\dagger}$ with

$$U=\frac{1}{\sqrt{2}}\begin{pmatrix} 1 & -\mathrm{i} \\ 1 & \mathrm{i} \end{pmatrix}. \tag{2}$$

The reflection matrix in the circular basis becomes

$$\tilde{R}(0)=\begin{pmatrix} r_{++} & r_{+-} \\ r_{-+} & r_{--} \end{pmatrix}. \tag{3}$$

In $r_{\alpha\beta}$, the first subscript denotes the reflected state and the second denotes the incident state, with $\alpha,\ \beta\in\{+,-\}$. Throughout this work, diagonal and off-diagonal channels refer to this fixed circular basis.

The positive orientation angle ϕ is defined by a right-handed rotation about the laboratory $+z$ axis, corresponding to counterclockwise rotation when viewed from the $+z$ side toward the origin. Within the local Jones-matrix description, rotation of the meta-atom gives

$$\begin{aligned}\tilde{R}(\phi) &= \begin{pmatrix} \mathrm{e}^{-\mathrm{i}\phi} & 0 \\ 0 & \mathrm{e}^{\mathrm{i}\phi} \end{pmatrix}\tilde{R}(0)\begin{pmatrix} \mathrm{e}^{\mathrm{i}\phi} & 0 \\ 0 & \mathrm{e}^{-\mathrm{i}\phi} \end{pmatrix} \\ &= \begin{pmatrix} r_{++} & r_{+-}\mathrm{e}^{-\mathrm{i}2\phi} \\ r_{-+}\mathrm{e}^{\mathrm{i}2\phi} & r_{--} \end{pmatrix}. \end{aligned} \tag{4}$$

The diagonal coefficients r_{++} and r_{--} acquire no rotation-dependent phase, whereas the off-diagonal coefficients r_{+-} and r_{-+} acquire PB phases of -2ϕ and $+2\phi$, respectively. Under the propagation convention adopted here, the off-diagonal channels preserve the propagation-referenced circular handedness, whereas the diagonal channels reverse it.

2.1. HWP-like and QWP-like limits

For a conventional birefringent unit cell with negligible cross coupling in the linear polarization basis, $r_{uv}=r_{vu}=0$. The polarization response is then determined by r_{uu} and r_{vv}. For an ideal HWP limit, the two principal-axis reflection amplitudes are matched and their phase difference is π, namely, $r_{uu}=-r_{vv}$. The rotated reflection matrix in the circular polarization basis becomes

$$\tilde{R}_{\mathrm{HWP}}(\phi)=r_{uu}\begin{pmatrix} 0 & \mathrm{e}^{-\mathrm{i}2\phi} \\ \mathrm{e}^{\mathrm{i}2\phi} & 0 \end{pmatrix}. \tag{5}$$

The two incident circular states are therefore transformed as

$$\tilde{R}_{\mathrm{HWP}}(\phi)|+\rangle = r_{uu}\cdot\mathrm{e}^{\mathrm{i}2\phi}|-\rangle, \tag{6}$$

$$\tilde{R}_{\mathrm{HWP}}(\phi)|-\rangle = r_{uu}\cdot\mathrm{e}^{-\mathrm{i}2\phi}|+\rangle. \tag{7}$$

Thus, the HWP-like response converts between the two fixed laboratory-frame circular basis states and imparts conjugate PB phases of $\pm2\phi$.[37] Under the propagation and polarization conventions defined above, the $+\to-$ channel corresponds to LCP incidence and LCP reflection, whereas the $-\to+$ channel corresponds to RCP incidence and RCP reflection. For a rotation profile $\phi(x,y)=l\theta(x,y)/2$, where θ is the azimuthal coordinate, the two incident circular polarizations generate conjugate vortex wavefronts with topological charges $+l$ and $-l$.

For an ideal QWP limit, the two principal-axis reflection coefficients have equal amplitudes and a phase difference of $\pi/2$. Taking $r_{uu} = \mathrm{i}r_{vv}$, the rotated reflection matrix becomes

$$\tilde{R}_{\mathrm{QWP}}(\phi) = \frac{r_{uu}}{2}\begin{pmatrix} 1-\mathrm{i} & (1+\mathrm{i})\cdot \mathrm{e}^{-\mathrm{i}2\phi} \\ (1+\mathrm{i})\cdot \mathrm{e}^{\mathrm{i}2\phi} & 1-\mathrm{i} \end{pmatrix}. \tag{8}$$

Its action on the two circular states is

$$\tilde{R}_{\mathrm{QWP}}(\phi)|+\rangle = \frac{r_{uu}(1-\mathrm{i})}{2}|+\rangle + \frac{r_{uu}(1+\mathrm{i})}{2}\mathrm{e}^{\mathrm{i}2\phi}|-\rangle, \tag{9}$$

$$\tilde{R}_{\mathrm{QWP}}(\phi)|-\rangle = \frac{r_{uu}(1+\mathrm{i})}{2}\mathrm{e}^{-\mathrm{i}2\phi}|+\rangle + \frac{r_{uu}(1-\mathrm{i})}{2}|-\rangle. \tag{10}$$

For LCP incidence, the diagonal contribution is an RCP reflected background, while the off-diagonal contribution is an LCP reflected vortex carrying the phase $+2\phi$. For RCP incidence, the corresponding outputs are an LCP background and an RCP vortex carrying the phase -2ϕ. Under the ideal QWP condition, the two components carry equal reflected powers; therefore, 50% of the reflected power lies in the PB-modulated channel. The efficiency relative to incident power is additionally limited by the total reflectance.[38–41]

2.2. Chiral-EP limit

We next consider a reciprocal but lossy anisotropic meta-atom with in-plane asymmetry.[30] For normal-incidence reflection from the reciprocal structure considered here, using the same transverse linear axes for the incident and reflected fields gives $r_{uv} = r_{vu}$. The reflection matrix in the fixed circular basis then becomes

$$\begin{aligned}\tilde{R}(0) &= \begin{pmatrix} \frac{1}{2}(r_{uu}+r_{vv}) & \frac{1}{2}(r_{uu}-r_{vv}) - \mathrm{i}r_{uv} \\ \frac{1}{2}(r_{uu}-r_{vv}) + \mathrm{i}r_{uv} & \frac{1}{2}(r_{uu}+r_{vv}) \end{pmatrix} \\ &= \begin{pmatrix} r_{++} & r_{+-} \\ r_{-+} & r_{--} \end{pmatrix}. \end{aligned} \tag{11}$$

The diagonal elements satisfy $r_{++} = r_{--}$. At an exceptional point, the two eigenvalues and eigenvectors coalesce, which requires $r_{+-}r_{-+} = 0$, with one of the two off-diagonal coefficients remaining nonzero. For the reciprocal system considered here, this condition gives

$$\frac{r_{uu}-r_{vv}}{2} = \pm\mathrm{i}r_{uv}. \tag{12}$$

The two signs correspond to opposite chiral-EP branches. For $(r_{uu}-r_{vv})/2 = \mathrm{i}r_{uv}$, $r_{+-} = 0$ and $r_{-+} \neq 0$; for $(r_{uu}-r_{vv})/2 = -\mathrm{i}r_{uv}$, $r_{-+} = 0$ and $r_{+-} \neq 0$. A nonzero surviving off-diagonal coefficient is essential, because a scalar matrix with both off-diagonal coefficients equal to zero is not an EP. Thus, one type of chiral-EP response can be represented by the lower-triangular Jordan form[42,43]

$$\tilde{R}_{\mathrm{EP}}(0) = \begin{pmatrix} r_{++} & 0 \\ r_{-+} & r_{++} \end{pmatrix}. \tag{13}$$

This form permits conversion from $|+\rangle$ to $|-\rangle$, while the opposite conversion from $|-\rangle$ to $|+\rangle$ vanishes. After rotating the unit cell by an angle ϕ, the reflection matrix becomes

$$\tilde{R}_{\mathrm{EP}}(\phi) = \begin{pmatrix} r_{++} & 0 \\ r_{-+}\cdot \mathrm{e}^{\mathrm{i}2\phi} & r_{++} \end{pmatrix}. \tag{14}$$

Its action on the circular states is

$$\tilde{R}_{\mathrm{EP}}(\phi)|+\rangle = r_{++}|+\rangle + r_{-+}\cdot \mathrm{e}^{\mathrm{i}2\phi}|-\rangle, \tag{15}$$

$$\tilde{R}_{\mathrm{EP}}(\phi)|-\rangle = r_{++}|-\rangle. \tag{16}$$

For the EP branch considered here, LCP incidence excites an LCP reflected component through r_{-+}, carrying the PB phase $+2\phi$, together with an RCP background through r_{++}. Under RCP incidence, the PB-modulated RCP component vanishes because $r_{+-} = 0$, while an LCP background remains if $r_{++} \neq 0$. Thus, the EP suppresses one PB-modulated conversion channel without necessarily eliminating the total reflection for that incident polarization.[34,44]

2.3. Numerical methods and meta-atom designs

The electromagnetic responses of the proposed meta-atoms and metasurfaces were numerically investigated using the finite-difference time-domain (FDTD) method. For the simulations of individual meta-atoms, periodic boundary conditions were applied in the x- and y-directions, while perfectly matched layers (PMLs) were used along the z-direction. The structures were excited by a normally incident plane wave propagating along the z-axis. The linear-polarization reflection coefficients were extracted from the reflected fields and subsequently transformed into the circular-polarization basis to obtain the co- and cross-polarized reflection responses. Wavelength-dependent optical parameters were used for the metallic materials. For the finite metasurface simulations, open boundaries terminated by PMLs were employed, and the polarization-resolved reflected fields were extracted to characterize the phase and intensity distributions of the generated optical vortices.

2.4. HWP-like and QWP-like meta-atoms

To realize the HWP-like and QWP-like responses described above, we employ reflective metal–insulator–metal (MIM) meta-atoms operating at $\lambda_0 = 600$ nm. As illustrated in Fig. 1(a), the structure consists of a metallic ground plane, a SiO_2 spacer, and a rectangular metallic nanoantenna. The unit-cell period is $P = 300$ nm. For the HWP-like and QWP-like designs, Ag is used for the top nanoantenna and bottom reflector, with layer thicknesses of $h_1 = 150$ nm, $h_2 = 80$ nm, and $h_3 = 30$ nm.[45]

A rectangular top antenna provides two independent principal-axis responses. For the HWP-like meta-atom, the optimized dimensions are $L = 186$ nm and $W = 84$ nm. At 600 nm, the reflection amplitudes satisfy $|r_{xx}| \approx |r_{yy}|$, while the phase retardation is $\Delta\varphi = \varphi_{xx} - \varphi_{yy} \approx \pi$.

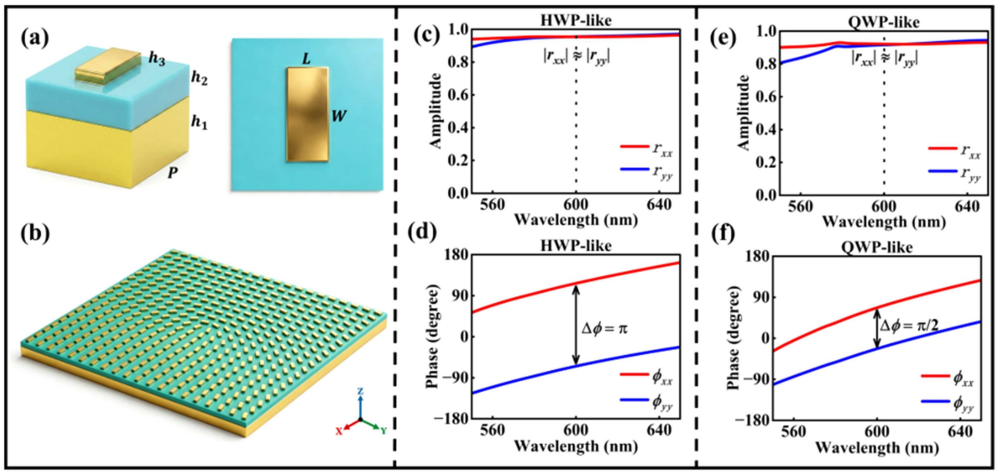

Fig. 1. Designs and spectral responses of the HWP-like and QWP-like metasurfaces. (a) Three-dimensional and top views of the reflective MIM meta-atom composed of a thick Ag ground plane, a SiO_2 spacer, and a rectangular Ag nanoantenna. (b) Schematic of the 20×20 PB metasurface for generating a first-order optical vortex. (c), (d) Principal-axis reflection amplitudes and phases of the optimized HWP-like meta-atom, showing an approximately π phase retardation at 600 nm. (e), (f) Corresponding responses of the QWP-like meta-atom, showing an approximately $\pi/2$ phase retardation at 600 nm.

For the QWP-like meta-atom, the dimensions are changed to $L = 130$ nm and $W = 100$ nm. The two principal-axis reflection amplitudes remain comparable, while the phase retardation is adjusted to approximately $\Delta\varphi \approx \pi/2$. This response produces simultaneous diagonal and off-diagonal reflection contributions in the fixed circular basis, corresponding to a background and a PB-modulated vortex with opposite reflected circular polarizations.

2.5. Chiral-EP meta-atom

To realize the non-Hermitian exceptional-point response, the top structure is designed as an asymmetric coupled resonator composed of an L-shaped antenna and a rectangular antenna, as shown in Fig. 2(a). Aluminum is used as the metallic material because of its relatively strong optical loss in the visible range. To enhance the coupling between the top resonator and the bottom reflector, the SiO_2 spacer thickness is reduced to $h_2 = 40$ nm. The period remains $P = 300$ nm, and the optimized geometrical parameters are $L_1 = 52$ nm, $L_2 = 140$ nm, $L_3 = 121$ nm, $w = 50$ nm, $g = 70$ nm. Here, L_1 and L_2 denote the two arm lengths of the L-shaped antenna, L_3 is the length of the rectangular antenna, w is the antenna width, and g is the gap between the two coupled resonators.

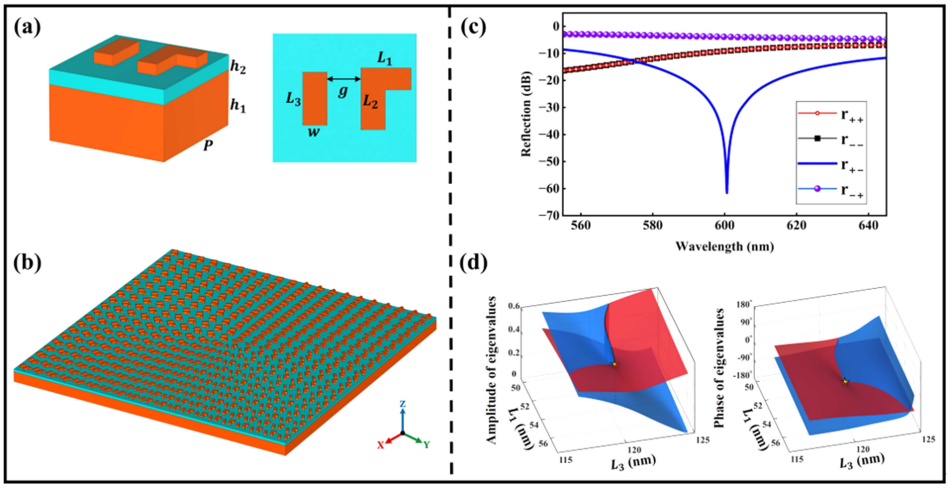

Fig. 2. Design and characterization of the chiral-EP metasurface. (a) Three-dimensional and top views of the reflective asymmetric meta-atom composed of an L-shaped Al antenna and a rectangular Al antenna. (b) Schematic of the 20×20 metasurface with the spatial orientation profile required for a first-order vortex. (c) Circular-basis reflection spectra of the optimized meta-atom. (d) Complex-eigenvalue surfaces of the local reflection Jones matrix in the (L_1, L_3) parameter space at 600 nm; the marked point denotes the optimized structure operating near the EP.

The circular-basis spectra of the asymmetric Al meta-atom are shown in Fig. 2(c). Near $\lambda_0 = 600$ nm, the two off-diagonal reflection coefficients are strongly unequal: r_{-+} remains finite, whereas r_{+-} is substantially suppressed. Meanwhile, the two complex eigenvalues of the reflection matrix approach each other near the optimized structural parameters, as shown in Fig. 2(d). The near-degeneracy of the eigenvalues, together with the nearly triangular circular-basis reflection

matrix, is consistent with operation in the vicinity of an exceptional point. This asymmetric coupled-resonator configuration therefore enables chiral scattering with strongly unbalanced off-diagonal channels, providing the basis for spin-selective PB-phase modulation.

3. Optical-vortex generation and comparison

3.1. Conjugate vortex generation by the HWP-like metasurface

Based on the HWP-like unit cell, we first construct a PB phase metasurface for generating a first-order optical vortex beam. For a vortex beam with topological charge l, the target phase distribution is $\varphi_l(\theta) = l\theta$ where θ is the azimuthal angle in the transverse plane. According to the PB phase relation $\varphi_{\mathrm{PB}}(r) = \pm 2\phi(r)$, the rotation angle of each unit cell is designed as $\phi(\theta) = l\theta/2$.

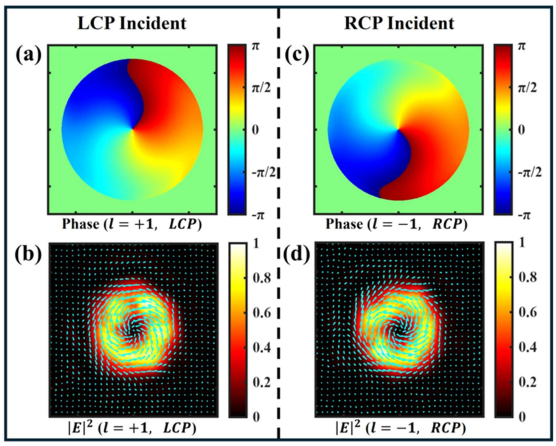

Fig. 3. Conjugate vortex generation by the HWP-like metasurface. (a) Phase of the LCP reflected component under LCP incidence, associated with the $+ \rightarrow -$ channel and a topological charge of $l = +1$. (b) Corresponding normalized intensity. (c) Phase of the RCP reflected component under RCP incidence, associated with the $- \rightarrow +$ channel and $l = -1$. (d) Corresponding normalized intensity. Topological-charge signs are defined in the fixed laboratory transverse coordinates.

Figure 3 shows the simulated reflected fields under the two incident spin states. For LCP incidence, the dominant reflected component arises from the $+ \rightarrow -$ channel and remains LCP under the propagation-referenced convention defined above. Its phase winds by 2π around the beam axis, corresponding to a topological charge of $l = +1$ [Fig. 3(a)]. The associated intensity has a central minimum and an annular profile [Fig. 3(b)]. For RCP incidence, the dominant reflected component arises from the $- \rightarrow +$ channel and remains RCP. Its phase winding reverses, corresponding to $l = -1$ [Fig. 3(c)], while the intensity retains an annular vortex profile [Fig. 3(d)].

The HWP-like metasurface therefore generates a pair of conjugate vortex wavefronts under opposite incident circular polarizations. The diagonal reflection coefficients r_{++} and r_{--} in the fixed circular basis are small near the design wavelength, resulting in a weak unmodulated background.

3.2. Polarization-split vortex generation by the QWP-like metasurface

The vortex-generation mechanism of the QWP-like metasurface is different from that of the half-wave-plate metasurface. The QWP-like metasurface supports both diagonal and off-diagonal reflection channels in the fixed circular basis. Under circularly polarized incidence, the reflected field therefore contains a background without rotation-induced PB phase and a PB-modulated vortex. These two components have opposite circular handedness.

Under LCP incidence, the RCP reflected component originates from r_{++} and forms a non-vortex background [Figs. 4(a) and 4(b)]. The LCP reflected component originates from r_{-+}, acquires the phase $+2\phi = +\theta$, and forms an $l = +1$ vortex [Figs. 4(c) and 4(d)]. Under RCP incidence, the LCP reflected component originates from r_{--} and forms the background [Figs. 4(e) and 4(f)], whereas the RCP reflected component originates from r_{+-}, acquires the phase $-2\phi = -\theta$, and forms an $l = -1$ vortex [Figs. 4(g) and 4(h)].

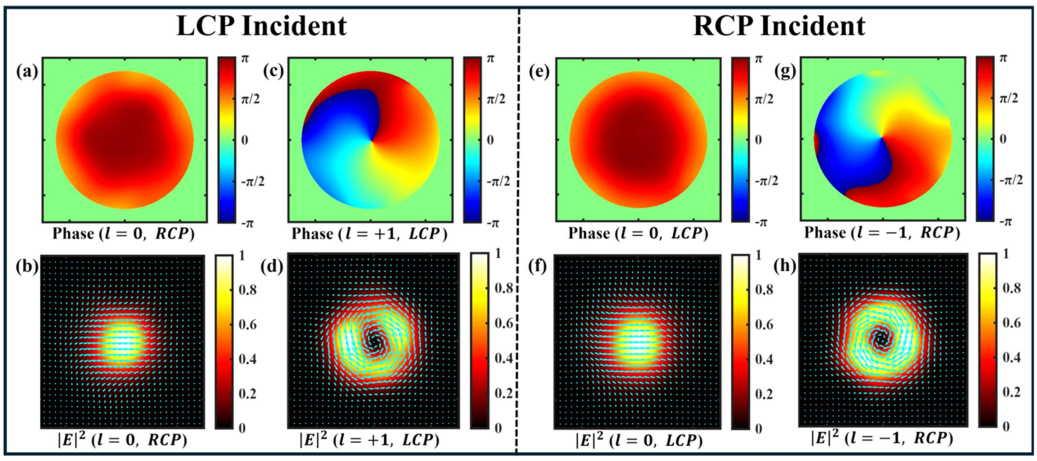

Fig. 4. Polarization splitting and vortex generation by the QWP-like metasurface. (a), (b) Phase and normalized intensity of the RCP reflected background under LCP incidence. (c), (d) Phase and normalized intensity of the LCP reflected vortex under LCP incidence, with $l = +1$. (e), (f) Phase and normalized intensity of the LCP reflected background under RCP incidence. (g), (h) Phase and normalized intensity of the RCP reflected vortex under RCP incidence, with $l = -1$.

The background contribution is intrinsic to the ideal QWP condition and limits the fraction of reflected power available in the PB-modulated vortex channel.

3.3. Spin-selective vortex generation near the chiral-EP

We further use the chiral-EP unit cell to construct a spin-selective PB phase metasurface. Owing to the in-plane asymmetric coupling and the material loss of aluminum, the designed unit cell exhibits a chiral scattering response near the working wavelength. The non-Hermitian metasurface uses the same orientation profile as the HWP and QWP arrays.

Figures 5(a)–5(c) characterize the reflection channels and eigenstate properties of the reflection Jones matrix in the two-dimensional structural-parameter space (L_1, L_3). Near the optimized parameters, the off-diagonal coefficient r_{+-} is strongly suppressed [Fig. 5(a)], while the phase rigidity exhibits a pronounced minimum [Fig. 5(b)], consistent with operation near a chiral exceptional point. Meanwhile, the opposite off-diagonal coefficient r_{-+} remains finite [Fig. 5(c)], enabling strongly asymmetric access to the PB-modulated channels. As the meta-atom is rotated through an in-plane angle ϕ, the amplitude of r_{-+} remains nearly constant, while its phase approximately follows the expected $+2\phi$ dependence [Fig. 5(d)]. With the orientation profile $\phi(x,y) = \theta(x,y)/2$, where θ denotes the spatial azimuthal angle, LCP incidence excites an LCP reflected component through r_{-+} under the propagation-referenced handedness convention adopted here. This component acquires the geometric phase $2\phi = \theta$, producing an $l = +1$ vortex with a 2π phase winding [Fig. 5(e)] and a central intensity minimum [Fig. 5(f)]. Under RCP incidence, the r_{+-} channel is strongly suppressed, inhibiting efficient generation of the conjugate vortex. This suppression applies to the PB-modulated channel and does not necessarily eliminate the total reflected field, which may retain a background through the diagonal reflection channel. The near-chiral-EP metasurface thus combines geometric-phase encoding with incident-spin-selective access to the vortex-generating channel.

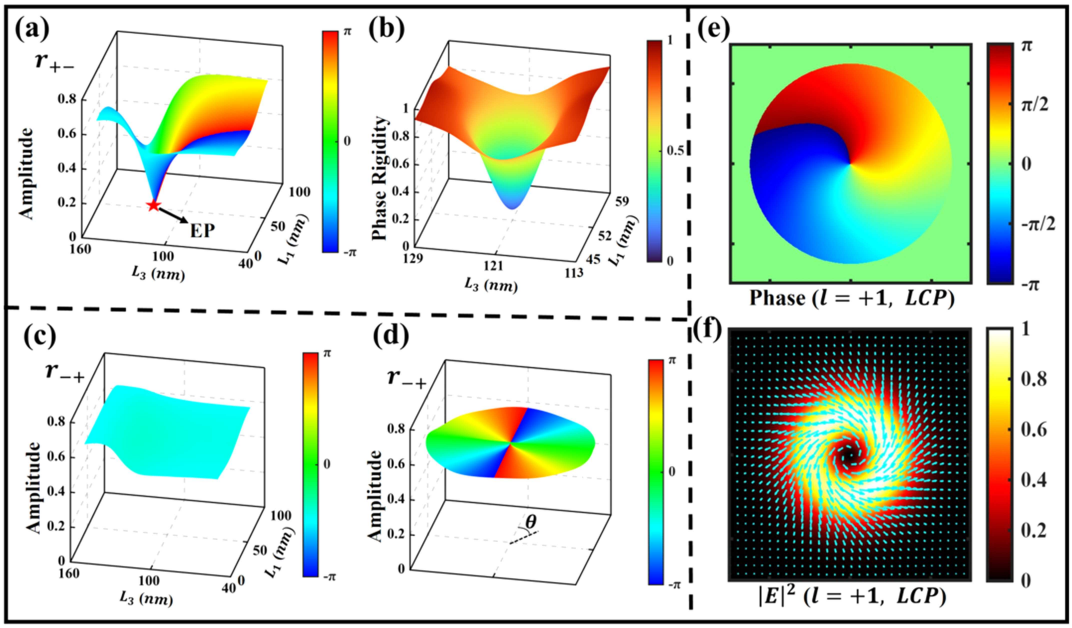

Fig. 5. Spin-selective PB-phase evolution and vortex generation near the chiral-EP. (a) Amplitude and phase evolution of r_{+-} in the structural-parameter space (L_1, L_3). (b) Corresponding phase rigidity mapping. (c) Amplitude and phase evolution of r_{-+} in the structural-parameter space (L_1, L_3). (d) Amplitudes and phases of r_{-+} as functions of the in-plane rotation angle. (e) Phase of the LCP reflected component under LCP incidence, showing an $l = +1$ vortex. (f) Corresponding normalized intensity.

3.4. Comparison of the three PB-phase mechanisms

Although the three metasurface systems obey the same rotation-induced PB-phase rule in Eq. (4), their different circular-basis scattering responses lead to distinct mechanisms for optical-vortex generation.

For the HWP-like metasurface, the off-diagonal channels dominate and generate conjugate vortices under opposite circularly polarized incidences. For the QWP-like metasurface, diagonal and off-diagonal channels coexist, producing a non-vortex background and a PB-modulated vortex with orthogonal circular polarizations. Near the chiral EP, one off-diagonal channel remains finite while the other is strongly suppressed, providing selective access to the PB phase for one incident circular polarization. The key differences among the three PB-phase mechanisms are summarized in Table 1.

Thus, the HWP-like and QWP-like metasurfaces provide spin-dependent PB-phase encoding, whereas the non-Hermitian EP further introduces spin-channel selectivity, extending PB-phase engineering from spin-dependent to spin-selective wavefront control.

Table 1. Mechanism-level comparison of the three reflective PB metasurfaces.

System	Approximate local condition	Access to PB phase	Main vortex response
HWP-like	$r_{uv} = r_{vu} = 0$ $r_{uu} = -r_{vv}$	Both spins	Conjugate vortices with $l = \pm 1$
QWP-like	$r_{uv} = r_{vu} = 0$ $r_{uu} = \mathrm{i} r_{vv}$	Both spins	Conjugate vortices accompanied by orthogonally polarized non-vortex backgrounds
Chiral-EP	$r_{uv} = r_{vu} \neq 0$ $(r_{uu} - r_{vv})/2 = \pm \mathrm{i} r_{uv}$	Selected spin	Spin-selective PB-modulated vortex

Table 2. Quantitative performance comparison of the HWP-like, QWP-like, and near-chiral-EP metasurface designs.

Regime	Incident	Total reflectance	PCR	SER	Target OAM purity	Relative bandwidth
HWP-like	LCP	90.8%	100%	0 dB	99.2%	21.3%
	RCP	90.8%	100%		99.1%	
QWP-like	LCP	84.6%	49.1%	0 dB	94.0%	26.5%
	RCP	84.6%	49.1%		93.8%	
Chiral-EP	LCP	53.5%	76.6%	53.8 dB	99.9%	4.2%

We also provide a quantitative comparison of the HWP-like, QWP-like, and near-EP designs in Table 2, including the spin extinction ratio, polarization conversion ratio, total reflectance, target orbital angular momentum (OAM) purity, and relative operational bandwidth. The spin extinction ratio (SER) compares the two off-diagonal reflection channels under equal incident powers and is defined as SER $= 10\log_{10}(|r_{-+}|^2/|r_{+-}|^2)$. The polarization conversion ratio (PCR) is defined as the power in the selected off-diagonal reflected channel divided by the total reflected power, including both circular-polarization components. The total reflectance is the total reflected power normalized to the incident power. The target OAM purity is defined as the fraction of power within the selected circular-polarization component carried by the target azimuthal order, determined through azimuthal OAM decomposition with radial integration.

4. Conclusion and perspectives

In conclusion, we have established a unified Jones-matrix framework for PB-phase generation in reflective HWP-like, QWP-like, and chiral-EP metasurfaces. In a fixed laboratory-frame circular basis, the rotation-induced PB phase appears in the off-diagonal reflection channels, while the diagonal channels carry no such phase. Under the adopted propagation convention, the PB-modulated reflected component preserves the incident circular handedness. The HWP-like metasurface generates conjugate vortices under opposite circularly polarized incidences, whereas the QWP-like metasurface produces vortices accompanied by orthogonally polarized backgrounds. Near the chiral EP, strong imbalance between the two off-diagonal channels enables incident-spin-selective vortex generation. These results connect birefringent and non-Hermitian reflective metasurfaces within a common framework and identify incident-spin selectivity as an additional degree of freedom for geometric-phase wavefront control.

Data availability statement

The data underlying the results presented in this paper are not publicly available at this time but may be obtained from the authors upon reasonable request.

Acknowledgements

This work was supported by the Natural Science Foundation of Zhejiang Province (Grant No. LY24A040001) and the Ningbo Youth Science and Technology Innovation Leading Talent Project (Grant No. 2023QL001).

References

[1] Yu N, Genevet P, Kats M A, Aieta F, Tetienne J, Capasso F and Gaburro Z 2011 *Science* **334** 333
[2] Kildishev A V, Boltasseva A and Shalaev V M 2013 *Science* **339** 1232009
[3] Bao Y, Nan F, Yan J, Yang X, Qiu C and Li B 2022 *Nat. Commun.* **13** 7550
[4] Mei F, Han J, Mao J, Sha X and Hu J 2025 *Opt. Commun.* **577** 131367
[5] Chen H, Taylor A J and Yu N 2016 *Rep. Prog. Phys.* **79** 076401
[6] Kuznetsov A I, Miroshnichenko A E, Brongersma M L, Kivshar Y S and Luk'yanchuk B 2016 *Science* **354** aag2472
[7] Zheng G, Mühlenbernd H, Kenney M, Li G, Zentgraf T and Zhang S 2015 *Nat. Nanotechnol.* **10** 308
[8] Yuan Y, Zhang K, Ratni B, Song Q, Ding X, Wu Q, Burokur S N and Genevet P 2020 *Nat. Commun.* **11** 4186
[9] Ji J, Li J, Wang Z, Li X, Sun J, Wang J, Fang B, Chen C, Ye X, Zhu S and Li T 2024 *Nat. Commun.* **15** 8271
[10] Maguid E, Yulevich I, Veksler D, Kleiner V, Brongersma M L and Hasman E 2016 *Science* **352** 1202
[11] Berry M V 1984 *Proc. R. Soc. A* **392** 45
[12] Bao Y, Wen L, Chen Q, Qiu C and Li B 2021 *Sci. Adv.* **7** eabh0365
[13] Jin X, He Y, Li J, Nie X, Du S, Song Y, Luo H, Liu M, Ma S, He Q, Zhou L, Wang Z and Sun S 2026 *Light Sci. Appl.* **15** 256
[14] He Y, Liu Y, Yao Y, Cai Q, Zhang D, Jin X, Sun S, Wang Z and Zhou L 2026 *Small* **22** e74309
[15] Wang Z, Pan W, He Y, Zhu Z, Jin X, Liu M, Ma S, He Q, Sun S and Zhou L 2025 *Opto-Electron. Sci.* **4** 240024
[16] Cao Q, Zhang N, Chong A and Zhan Q 2024 *Nat. Commun.* **15** 7821
[17] Bliokh K Y, Rodríguez-Fortuño F J, Nori F and Zayats A V 2015 *Nat. Photonics* **9** 796
[18] Allen L, Beijersbergen M W, Spreeuw R J C and Woerdman J P 1992 *Phys. Rev. A* **45** 8185
[19] Yao A M and Padgett M J 2011 *Adv. Opt. Photonics* **3** 161
[20] Forbes A, de Oliveira M and Dennis M R 2021 *Nat. Photonics* **15** 253

[21] Shen Y, Wang X, Xie Z, Min C, Fu X, Liu Q, Gong M and Yuan X 2019 *Light Sci. Appl.* **8** 90

[22] He H, Tang S, Zheng Z and Ding F 2022 *Opt. Lett.* **47** 2478

[23] Zhu Y, Zhou S, Wang Z, Pu X, Cao X, Yu Y, Yuan W and Liu W 2021 *Results Phys.* **29** 104765

[24] Chen Q, Qu G, Yin J, Wang Y, Ji Z, Yang W, Wang Y, Yin Z, Song Q, Kivshar Y and Xiao S 2024 *Nat. Nanotechnol.* **19** 1000

[25] Huang L, Chen X, Mühlenbernd H, Zhang H, Chen S, Bai B, Tan Q, Jin G, Cheah K, Qiu C, Li J, Zentgraf T and Zhang S 2013 *Nat. Commun.* **4** 2808

[26] Arbabi A, Horie Y, Bagheri M and Faraon A 2015 *Nat. Nanotechnol.* **10** 937

[27] Qin H, Lv W, Wang J, Sun K, Mu X, Han Z, Song Q and Qiu C 2026 *Phys. Rev. Lett.* **136** 183805

[28] Li A, Wei H, Cotrufo M, Chen W, Mann S, Ni X, Xu B, Chen J, Wang J, Fan S, Qiu C, Alù A and Chen L 2023 *Nat. Nanotechnol.* **18** 706

[29] Shou Y, Wang D, Wang Y, Huang Q, Chen H, Yu W, Ju R, Chen H and Li Y 2025 *npj Nanophotonics* **2** 29

[30] Miri M and Alù A 2019 *Science* **363** eaar7709

[31] Yi C, Wang Z, Shi Y, Wan S, Tang J, Hu W, Li Z, Zeng Y, Song Q and Li Z 2025 *Light Sci. Appl.* **14** 262

[32] Song Q, Odeh M, Zúñiga-Pérez J, Kanté B and Genevet P 2021 *Science* **373** 1133

[33] Park J, Ndao A, Cai W, Hsu L, Kodigala A, Lepetit T, Lo Y and Kanté B 2020 *Nat. Phys.* **16** 462

[34] Yang Z, Huang P, Lin Y, Qin H, Zúñiga-Pérez J, Shi Y, Wang Z, Cheng X, Tang M, Han S, Kanté B, Li B, Wu P C, Genevet P and Song Q 2024 *Nat. Commun.* **15** 232

[35] Lyu Q, Yan Q, Zhao W, Chu S, Hu X and Gong Q 2026 *Nat. Commun.* **17** 3991

[36] Ding F, Deng Y, Meng C, Thrane P C V and Bozhevolnyi S I 2024 *Sci. Adv.* **10** eadl4661

[37] Lin D, Fan P, Hasman E and Brongersma M L 2014 *Science* **345** 298

[38] Marrucci L, Manzo C and Paparo D 2006 *Phys. Rev. Lett.* **96** 163905

[39] Guo Y, Zhang S, Pu M, He Q, Jin J, Xu M, Zhang Y, Gao P and Luo X 2021 *Light Sci. Appl.* **10** 63

[40] Liu M, Huo P, Zhu W, Zhang C, Zhang S, Song M, Zhang S, Zhou Q, Chen L, Lezec H J, Agrawal A, Lu Y and Xu T 2021 *Nat. Commun.* **12** 2230

[41] Zeng J, Luk T S, Gao J and Yang X 2017 *Sci. Rep.* **7** 11824

[42] Kang M, Chen J and Chong Y D 2016 *Phys. Rev. A* **94** 033834

[43] Heiss W D 2012 *J. Phys. A: Math. Theor.* **45** 444016

[44] Wang S, Hou B, Lu W, Chen Y, Zhang Z Q and Chan C T 2019 *Nat. Commun.* **10** 832

[45] Sun S, Yang K, Wang C, Juan T, Chen W T, Liao C Y, He Q, Xiao S, Kung W, Guo G, Zhou L and Tsai D P 2012 *Nano Lett.* **12** 6223